A parameter-free LES model for anisotropic mesh adaptivity

J.E. Avalos-Patiño[*], S.J. Neethling, M.D. Piggott

Department of Earth Science & Engineering, Imperial College London, UK

Abstract

Balancing accuracy and computational cost is a challenge in the modelling of turbulent flows. A widely used method for turbulence modelling is large–eddy simulation (LES). LES allows one to describe large scale flow features at a reasonable computational cost compared to the more accurate direct numerical simulation (DNS), making it a popular choice for engineering applications. One strategy to balance accuracy and cost with LES is through the use of mesh adaptivity, which allows the degrees of freedom in a problem to be reduced by changing spatial discretisation. However, mesh adaptivity can affect accuracy when using the standard Smagorinsky LES model with an implicit filter, considering that the parameter C_s is highly dependent on the filter width, which depends on mesh resolution. This work is aimed to develop an LES model that does not require any user–defined parameters and is suitable for mesh adaptivity with implicit filter. In this study we introduce a parameter–free LES model incorporating an anisotropic eddy–viscosity formulation combined with anisotropic mesh adaptivity. In our model, the parameter C_s in the eddy–viscosity formulation of the Smagorinsky model, is replaced by a function that evaluates the relative location of turbulence fluctuations in each element with respect to the turbulence spectrum inertial range. The anisotropic formulation of the eddy–viscosity allows for the application of an appropriate filter width in different directions, improving accuracy. Additionally, the mesh adaptivity algorithm assesses the local turbulence fluctuations via local Reynolds number and vortex identification criteria. This assessment leads to the refinement of regions with higher turbulence fluctuations down to the smallest scale limit in the inertial range in the corresponding direction, and also leads to the coarsening of regions without turbulence fluctuation up to largest scale limit in the inertial range. This method is tested using a flow past a sphere test case. The results are compared both qualitatively and quantitatively to results obtained with the standard Smagorinsky model, and demonstrate the better performance of our method with lower computational cost. This allows us to simulate large Reynolds number cases and compare our quantitative results to experimental results found in the literature, emphasising that our method produces good results at reasonable computational cost.

© 2023 The Author(s). Published by Elsevier B.V. This is an open access article under the CC BY-NC-ND license (http://creativecommons.org/licenses/by-nc-nd/4.0/).

Keywords: Turbulence modelling; Large-eddy simulation; Anisotropic mesh adaptivity; Flow topology

1. Introduction

A number of different methods have been developed for simulating turbulent flows. The simplest and most accurate of these methods is direct numerical simulation (DNS). This method resolves all the turbulence scales down to the smallest scales, known as the Kolmogorov scale. However, DNS is the most computationally expensive method, requiring extremely high resolution in both space and time, making DNS unfeasible for many engineering

Nomenclature

C_D	Drag coefficient
C_s	Smagorinsky constant
D	Discriminant of the characteristic polynomial of the velocity gradient tensor
$D^\star$	Boundary layer between rotating and non–rotating flow
$\mathcal{D}$	Time scale operator
k	Wavenumber
ℓ	Subfilter–length scale
L	Integral scale
$\hat{\mathbf{n}}$	Outward normal vector
P	First invariant of the velocity gradient tensor
p	Pressure
Q	Second invariant of the velocity gradient tensor
R	Third invariant of the velocity gradient tensor
$R^\star$	Boundary layer between vortices and between flow and physical boundaries
$\overline{\overline{\mathcal{S}}}$	Strain–rate tensor
t	Time
$\mathbf{u}$	Velocity
$\overline{\mathbf{u}}$	Filtered velocity component
$\mathbf{u}'$	Residual velocity component

Greek symbols

Δ	Element size
η	Kolmogorov scale
Γ	Length scale operator
γ	Wall damping function
λ	Eigenvalues
ν	Kinematic viscosity
ν_τ	Eddy viscosity
ω	Quantity for the omega vortex identification method
$\overline{\overline{\Delta}}$	Filter–width
$\overline{\overline{\Omega}}$	Rotation–rate tensor
ψ	Reference scale within the inertial range of turbulence spectrum
ρ	Density
τ	Subfilter–scale stress tensor

applications [1]. Alternatively, approaches based on the Reynolds–averaged Navier–Stokes equations (RANS) are commonly used for engineering applications, given their low computational cost and simplicity compared to other methods. RANS methods were originally developed for steady state problems, therefore standard RANS approaches are incapable of capturing turbulent fluctuations [2]. Although different variants based on RANS, such as unsteady RANS (URANS) and very–large eddy simulation (VLES), have extended the capabilities of RANS, some limitations persist for different applications [2–5].

Another widely used method for turbulence modelling is large–eddy simulation (LES). LES allows the large scale flow features to be represented at a reasonable computational cost compared to DNS. The computational cost of turbulence modelling is related to the Reynolds number, as it defines the spatial discretisation resolution required to achieve good accuracy. For DNS, the spatial discretisation requires a number of nodes $n \sim Re^{9/4}$ to resolve the smallest scales. For LES the number of nodes required is much smaller, as only the larger scales are resolved,

whilst the smaller scales are 'modelled'. Grid resolution in LES is defined such that 80% of the energy is resolved, thus $n \sim Re$ in regions remote from walls (wall–modelled LES) and $n \sim Re^{9/5}$ in near–wall regions (wall–resolved LES) [6,7]. This is of interest for a wide variety of engineering problems as larger eddies are responsible for momentum and energy transfer and thus larger eddies are the most important ones for particle transport and heat transfer [4,8–10]. However LES can be inadequate for applications where phenomena occur at scales close to the Kolmogorov scale such as acoustics, mixing and chemical reactions which require resolving more than 80% of the energy [11,12].

The separation between large scales and small scales is defined by a filtering operation. The filter size can be defined as being proportional to the mesh size, therefore, turbulence modelling errors can be reduced by refining the mesh such that LES approaches DNS, however, this implies losing its computational cost advantage [13,14]. Additionally, the approximation error includes the discretisation errors, related to the order of accuracy of the discretisation scheme used for solving the governing equations, and the turbulence modelling errors, due to small scales which are not resolved [15,16]. An alternative to overcome this issue is adaptive meshing such that local mesh size is consistent with the turbulence length–scales according to the flow conditions [6].

Aristodemou et al. [17] developed a combined LES–mesh adaptive model, based on the Smagorinsky model [18], using an anisotropic eddy–viscosity formulation and finite element discretisation, to study micro–scale pollution transport. The implemented model showed good results in terms of accuracy at a lower computational cost compared to fixed mesh LES, as the adaptivity algorithm refined the regions with higher turbulent fluctuations and also coarsened regions with low turbulent fluctuations, leading to meshes with fewer nodes for a given accuracy. Despite the capabilities introduced by this model, it still uses a prescribed value of C_s for the small scale modelling that remains constant in space and time. Bull et al. [19] implemented a dynamic LES mesh adaptive model based on the model proposed by Aristodemou et al. [17] resulting in a 60% reduction in the number of nodes required whilst retaining good accuracy. However, the authors acknowledge that a parameter–free LES model with a reduced computational cost for complex industrial problems remains a challenge.

The aim of this work is to develop an LES model that does not require any user–defined parameters and which is suitable for use with mesh adaptivity, including fully accounting for mesh anisotropy. The resultant simulations therefore aim to improve the balance between the accuracy of the results and computational cost. The performance of this new model is assessed using a flow past a sphere test case. The results are compared both qualitatively and quantitatively to results obtained with the standard Smagorinsky model, using the drag coefficient and time–averaged stream–wise velocity as metrics for accuracy assessment and the maximum number of degrees of freedom reached during mesh adaptivity for computational cost assessment. This assessment demonstrates the better performance of our method with lower computational cost. This allows us to simulate large Reynolds number cases and compare our quantitative results to experimental results found in the literature, emphasising that our method produces good results at reasonable computational cost.

The layout of the article is as follows. Large–Eddy Simulation (LES) is introduced in Section 2, including an explanation of the relationship between LES and the turbulence spectrum. Section 3 presents the new parameter–free LES model developed in this work, including the anisotropic mesh adaptivity method based on flow topology implemented to complement the parameter–free eddy–viscosity formulation. The performance of the new turbulence model developed in this work is assessed quantitatively and qualitatively in Section 4 in a flow past a sphere test case. Finally, Section 5 presents the conclusions of this work

2. Large–Eddy simulation (LES)

Turbulent flows contain a wide range of scales related to energy transfer in the flow. Energy generally enters at the largest scales and is transferred continuously to smaller scales via an energy cascade until it is dissipated [6,15,20]. LES is based on the assumption that the largest scales are responsible for most of the energy transport, hence eddies at these scales are resolved, whilst smaller scale eddies, responsible for viscous dissipation, are modelled [9,21,22]. The scales separation is carried out by a filtering operation applied to the Navier–Stokes equations.

Consider the incompressible Navier–Stokes equations under the Boussinesq approximation:

$$\frac{\partial \mathbf{u}}{\partial t} + \mathbf{u} \cdot \nabla \mathbf{u} + \frac{1}{\rho} \nabla p - \nabla \cdot (\overline{\overline{\nu}} \nabla \mathbf{u}) = f, \tag{1}$$

$$\nabla \cdot \mathbf{u} = 0, \tag{2}$$

where $\mathbf{u}$ is the velocity vector, p is the pressure, $\overline{\overline{\nu}}$ is the kinematic viscosity, ρ is the density and f is an arbitrary source. Through the filtering operation the velocity field $\mathbf{u}$ is decomposed into a filtered component $\overline{\mathbf{u}}$ and a residual component $\mathbf{u}'$, such that $\mathbf{u} = \overline{\mathbf{u}} + \mathbf{u}'$. For brevity, we refer the reader to [6] and [15] for detailed explanation of the filtering operation. This yields the filtered equations:

$$\frac{\partial \overline{\mathbf{u}}}{\partial t} + \overline{\mathbf{u}} \cdot \nabla \overline{\mathbf{u}} + \frac{1}{\rho} \nabla \overline{p} - \nabla(2\overline{\overline{\nu}}\overline{\overline{\mathcal{S}}} - \tau) = \overline{f}, \tag{3}$$

$$\nabla \cdot \overline{\mathbf{u}} = 0, \tag{4}$$

with

$$\overline{\overline{\mathcal{S}}} = \frac{1}{2}(\nabla \overline{\mathbf{u}} + \nabla \overline{\mathbf{u}}^T), \tag{5}$$

$$\tau = \overline{\mathbf{u}\mathbf{u}} - \overline{\mathbf{u}}\,\overline{\mathbf{u}}, \tag{6}$$

where the single overbar denotes filtered quantities and τ is the residual or subfilter–scale stress tensor [15].

A formulation for τ is obtained from considering only its anisotropic part by assuming that its isotropic part is added to the pressure and that τ is aligned with the filtered strain–rate tensor $\overline{\overline{\mathcal{S}}}$:

$$\tau = -2\nu_\tau \overline{\overline{\mathcal{S}}}, \tag{7}$$

where ν_τ is the eddy–viscosity. This formulation of the subfilter–scale stress introduces a closure problem, hence, a formulation for ν_τ is required. A widely used expression for the eddy viscosity is given by the standard Smagorinsky model [18]:

$$\nu_\tau = \ell^2 \left| \overline{\overline{\mathcal{S}}} \right|, \tag{8}$$

where $\ell = C_s \overline{\Delta}$ is the subfilter–length scale, with C_s the Smagorinsky constant and $\overline{\Delta}$ the filter width.

In implicit LES, the filter width $\overline{\Delta}$ depends on the local element size Δ by the relation $\overline{\Delta} = \alpha \Delta$, with $\alpha \geq 1$ [20]. The value of α is related to the range of turbulent motions resolved. Lower values of α lead to resolve a larger range of turbulent motions, however it also yields poor numerical resolution [6,15]. A value of $\alpha = 2$ is recommended for reducing numerical errors [23]. The element size is usually calculated as $\Delta = A^{1/2}$ in 2D or $\Delta = V^{1/3}$ in 3D, where A and V are the local element area or volume respectively. Thus the eddy–viscosity takes the form:

$$\nu_\tau = (\alpha C_s \Delta)^2 \left| \overline{\overline{\mathcal{S}}} \right|. \tag{9}$$

This formulation does not account for anisotropy in the eddy–viscosity. Bentham [24] developed a tensorial form of the eddy–viscosity, accounting for proper subfilter–length scales in each direction for anisotropic meshes, by redefining the filter width $\overline{\Delta}$ as a tensor $\overline{\Delta}_{ij}$. The filter width tensor has the following form:

$$\overline{\Delta}_{ij} = \mathbf{V^T} \begin{bmatrix} \overline{\Delta}_\xi & 0 & 0 \\ 0 & \overline{\Delta}_\eta & 0 \\ 0 & 0 & \overline{\Delta}_\zeta \end{bmatrix} \mathbf{V} = \mathbf{V^T} \begin{bmatrix} \alpha \Delta_\xi & 0 & 0 \\ 0 & \alpha \Delta_\eta & 0 \\ 0 & 0 & \alpha \Delta_\zeta \end{bmatrix} \mathbf{V}, \tag{10}$$

where $\mathbf{V^T}$ and $\mathbf{V}$ are rotational matrices that transform the filter width from the local coordinate system (ξ, η, ζ) to a global coordinate system (x, y, z). Hence, the eddy–viscosity becomes:

$$\nu_\tau = \alpha^2 C_s^2 \left| \overline{\overline{\mathcal{S}}} \right| \Delta_{ij}^2. \tag{11}$$

Given this formulation, it is still necessary to define the value of C_s, which is an assumed input and has been shown to be unsuitable for certain flows [25]. Some values of C_s determined theoretically do not account for the flow properties and parameters, like the Reynolds number, that could make the value of C_s not constant [20]. Studies have been carried out to determine values of C_s for different flows experimentally [26–28] and theoretically [29–35]. Numerical experiments have shown that these determined values of C_s could be optimised and should be calibrated using experimental or observed data [15,36]. Additionally, C_s can vary widely and is highly dependent on the filter width $\overline{\Delta}$ [37,38]. Hence, C_s is highly dependant on the mesh resolution, given the implicit formulation of the filter width, $\overline{\Delta} = \alpha \Delta$.

2.1. Turbulence spectrum

At high Reynolds numbers, energy is transferred from large eddies to smaller eddies until the smallest scales at which energy is transferred as dissipation are reached [6]. This energy transfer phenomenon is usually known as the turbulent energy cascade and arises in a wide spectrum of flow scales. These flow scales are classified into three ranges within the turbulence spectrum:

(*i*) the production range, which includes large energy–containing eddies and is characterised by the integral scale;

(*ii*) the inertial range, where the energy cascade occurs following the so–called $-5/3$ power law, and

(*iii*) the dissipation range where viscous effects dissipate energy and is characterised by the scale of the smallest eddies, known as the Kolmogorov scale. Fig. 1 shows an schematic of the turbulence spectrum.
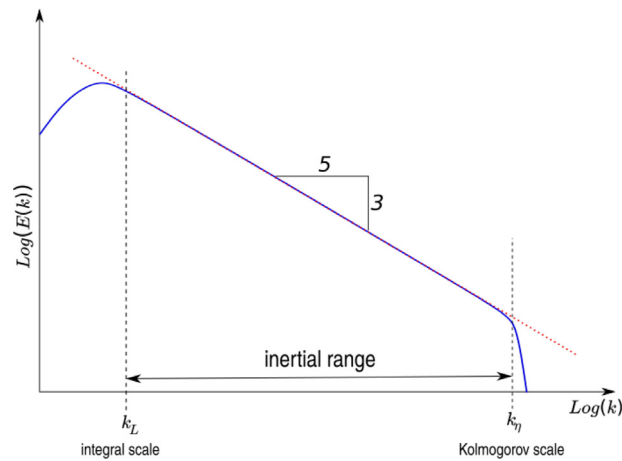
Fig. 1. Schematic of turbulent energy spectrum $E(k)$, where k is wavenumber. The inertial range is bounded by the wavenumbers corresponding to the integral scale k_L and the Kolmogorov scale k_η.

The capabilities of turbulence models can be explained in terms of the extent of the spectrum that can be resolved (see Fig. 2). The extent of the spectrum resolved also relates to the computational cost. Resolving a wider region of the spectrum requires a finer computational mesh, and implies a higher cost, as shown in Fig. 3.

In the case of LES, the extent of the spectrum that can be resolved spans the whole inertial range determined by the spatial discretisation. Coarse discretisations lead to lower computational cost, as some eddy structures are filtered out and are thus not directly resolved, but modelled as a function of the mean flow instead. Refined discretisations lead to higher computational cost, but smaller eddy structures are resolved, increasing accuracy. One strategy to balance accuracy and cost is mesh adaptivity as demonstrated by Bull et al. [19]. Fig. 4 explains the scale separation in LES and the effect on resolution and cost.

A known caveat of the Smagorinsky model is the over–estimation of the eddy–viscosity in high shear regions where eddy–viscosity should vanish, leading to an overly diffusive behaviour. This over estimation is due to the dependence of ν_τ on the operator $\left|\overline{\overline{\mathcal{S}}}\right|$. This caveat has been handled with the implementation of damping functions for near-wall regions [39], and dynamic methods for calculating C_s such that ν_τ goes to zero in those regions [25,40,41], aiming for the asymptotic behaviour of the eddy–viscosity in the near–wall region of a turbulent boundary layer, as in DNS. However, these approaches still require the use of constants as inputs for estimating ν_τ.

In the next section we introduce a novel method that couples an eddy–viscosity formulation, based on the Smagorinsky model, and dynamic anisotropic mesh adaptivity, based on flow topology. This coupling ensures that most of the turbulent flow structures are resolved, whilst balancing computational cost.
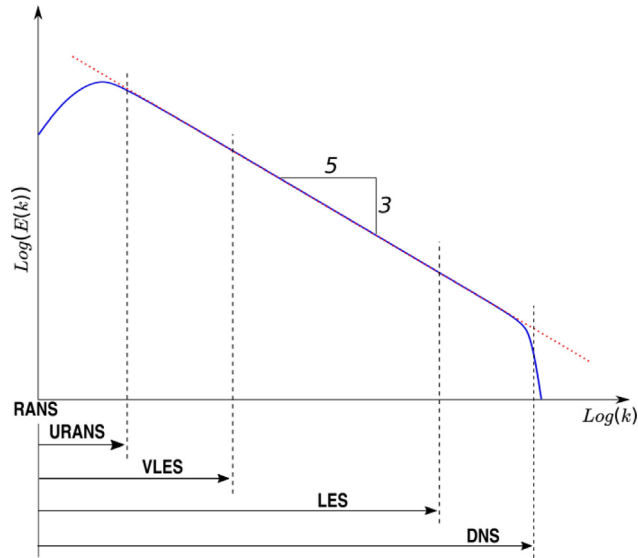
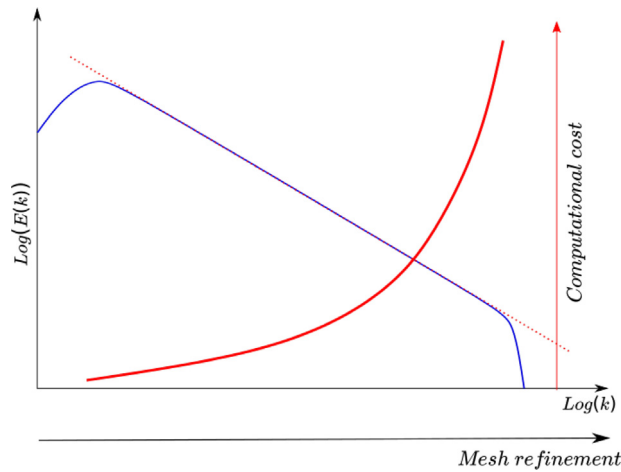**Fig. 2.** Extent of the turbulent energy spectrum resolved by different turbulence models.

Fig. 3. Schematic of the computational cost of LES across the turbulence spectrum extent that is resolved.

3. Parameter–free LES model

3.1. Parameter–free eddy–viscosity formulation

The eddy–viscosity can be defined in terms of a length scale operator Γ and a time scale operator $\mathcal{D}$, such that the eddy–viscosity is dimensionally consistent with the bulk viscosity. In the standard Smagorinsky model, the length scale operator is a function of the filter width:

$$\Gamma(\overline{\Delta}) = \ell^2 = (C_s \overline{\Delta})^2, \tag{12}$$

where ℓ is the subfilter–length scale, C_s is the Smagorinsky constant, and $\overline{\Delta} = \alpha \Delta$, with $\alpha \geq 1$ is the filter width. The time scale operator is related to velocity gradients $\mathcal{D} = \left|\overline{\overline{\mathcal{S}}}\right|$. This yields the eddy–viscosity formulation in the standard Smagorinsky model:

$$\nu_\tau = (C_s \overline{\Delta})^2 \left|\overline{\overline{\mathcal{S}}}\right|. \tag{13}$$

6

(a) Coarse discretisation   (b) Refined discretisation
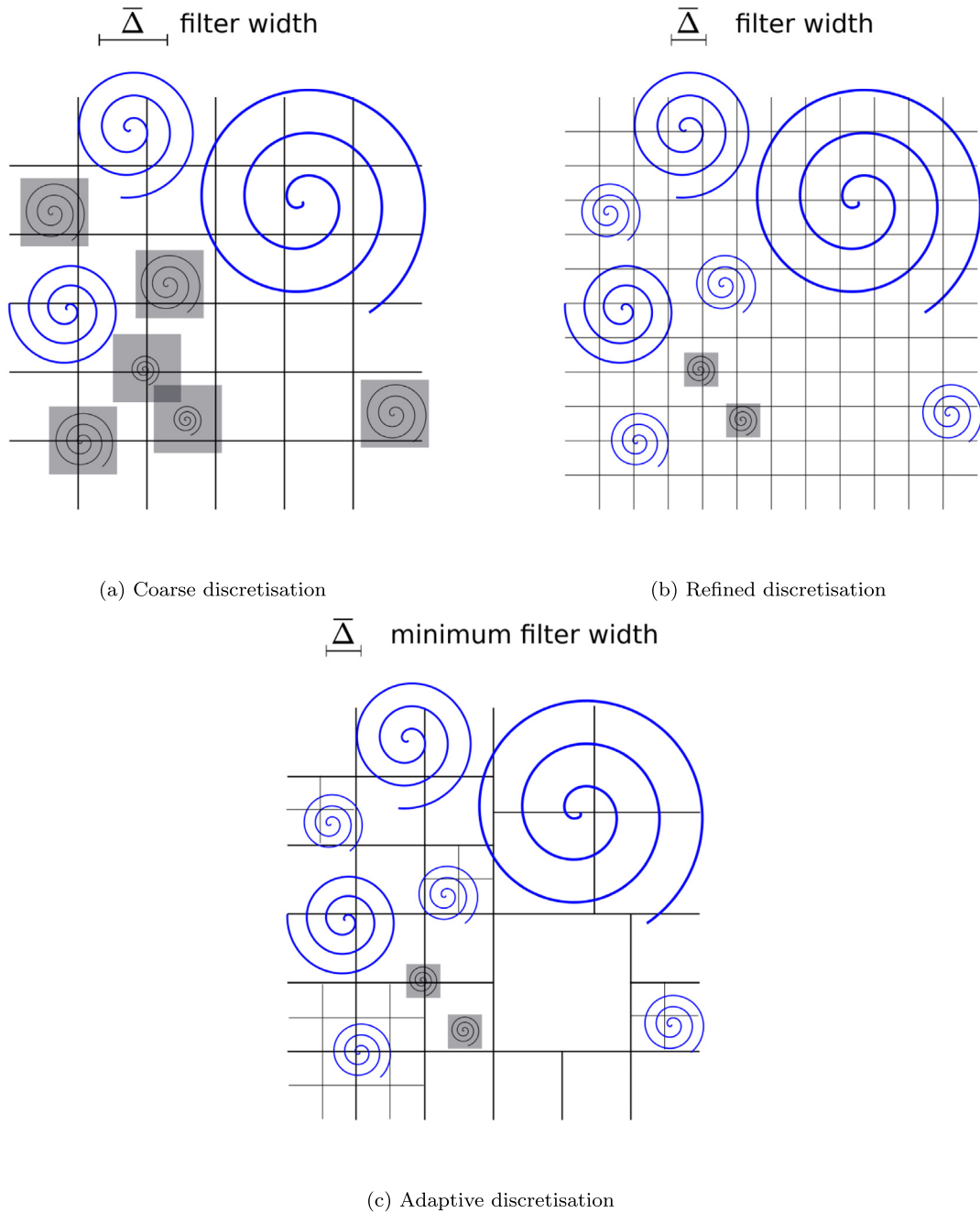
(c) Adaptive discretisation

Fig. 4. Schematic of the length scale separation in LES, showing the resolved eddies (blue) and the sub–filter scale eddies (in grey squares). The size of the squares is defined by the filter width for each discretisation with $\overline{\Delta} = \Delta x$: (a) coarse discretisation, only the largest eddies are resolved. (b) refined discretisation, most eddies are resolved and only the smallest eddies are modelled, however the degrees of freedom are increased leading to higher computational cost. (c) Adaptive discretisation, resolves the same number of eddies as the refined discretisation, but reduces the degrees of freedom by coarsening regions with fewer turbulent flow structures. The minimum grid element size is a parameter that controls the maximum resolution allowed for local refinement.

Previous studies, such as those performed by Van Driest [39], Moin and Kim [42] and Piomelli et al. [43], present methods aimed at overcoming the diffusive behaviour of the Smagorinsky model in near–wall regions. These methods typically involve two strategies:

(*i*) local refinement in the near–wall regions, and

(*ii*) models with modified formulations of the eddy–viscosity.

These models rely on multiplying the eddy–viscosity by a function $\gamma(x)$ such that $\gamma \to 0$ when $x \to 0$, with x being the distance to the wall. This function $\gamma(x)$ acts as a damping factor that ensures a consistent asymptotic behaviour of the eddy–viscosity and velocity field in regions near physical boundaries. Fig. 5 shows a schematic of the mentioned strategies.
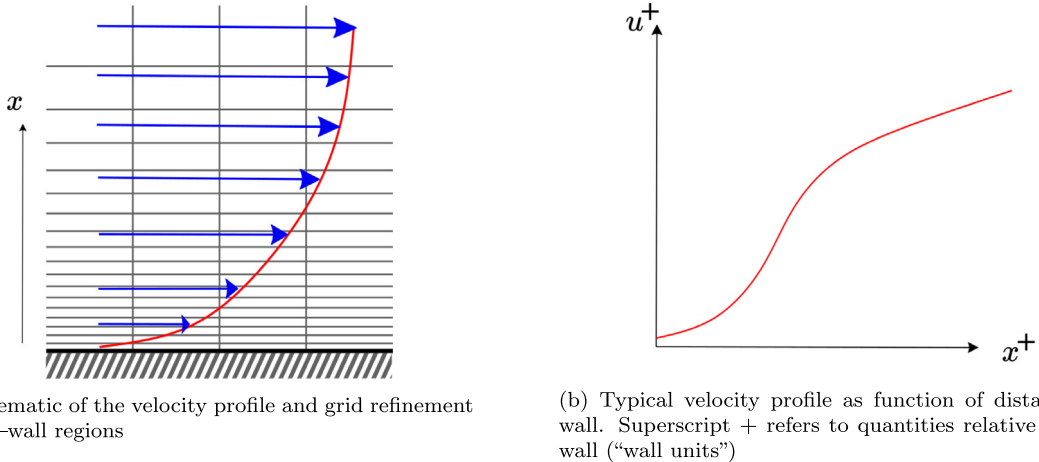

(a) Schematic of the velocity profile and grid refinement in near–wall regions

(b) Typical velocity profile as function of distance to wall. Superscript + refers to quantities relative to the wall ("wall units")

Fig. 5. Schematic of the typical strategies for addressing diffusive behaviour of LES models in near–wall regions.

A widely known formulation for the damping factor is $\gamma(x) = 1 - \exp(-x/A)$ proposed by Van Driest [39]. This formulation is based on the variation on the amplitude of fluid motion with respect to the distance to an oscillating wall. This variation was shown to have the form $\exp(-x/A)$ by Stokes [44], with x the distance from the wall and A a constant depending on the frequency of oscillation of fluid with respect to the wall and the kinematic viscosity of the fluid. This formulation of the damping factor leads to the expected behaviour of the eddy–viscosity and velocity, however, the use of this factor is limited to regions near physical boundaries. Given this limitation, the diffusive behaviour of the Smagorinsky model in high shear regions not associated with wall proximity needs to be addressed.

The new model introduced here aims to address the diffusive behaviour of the Smagorinsky model in high shear regions, not limited to near–wall regions. This is achieved by implementing the concept of damping factor in the turbulence spectrum domain, instead of the physical domain. The proposed damping factor makes use of the limits of the inertial range as bounds for the domain, instead of using physical walls, as implemented in the above–mentioned approaches. To ensure a consistent asymptotic behaviour of the eddy–viscosity and velocity field in high shear regions, this damping factor is defined such that the length scale operator $\Gamma(\overline{\Delta}) = \ell^2$ follows a sigmoid function going to zero in the limit of the Kolmogorov scale. A schematic of the relation of the length scale and turbulence spectrum is shown in Fig. 6.

In this new model, the length scale operator is defined as:

$$\Gamma(\overline{\Delta}) = \ell^2 = \phi \overline{\Delta}^2. \tag{14}$$

Here ϕ is the turbulence scales damping factor. This factor is a function of three scales of the turbulence spectrum within the inertial range $\phi = f(k_c, k_\eta, k_L)$, where $k_c = \pi/\overline{\Delta}$ is the cut–off filter wavenumber, $k_\eta \approx 1/\eta$ is the wavenumber corresponding to the Kolmogorov scale η, and $k_L \approx 1/L$ is the wavenumber corresponding to the integral length scale L. The asymptotic behaviour is achieved by defining ϕ as a sigmoid function:

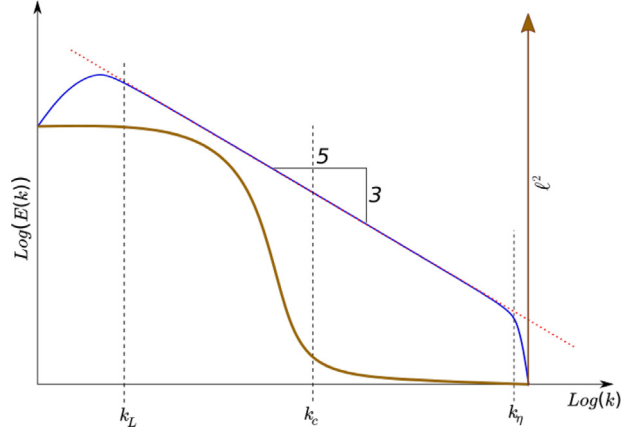$$\phi = \frac{\psi}{\psi + e^{k_c}}, \tag{15}$$

Fig. 6. Relation between turbulence spectrum and length scale *l*.

where ψ is a reference scale within the inertial range defined by a logarithmic mean of the integral and Kolmogorov scales:

$$\psi = \frac{k_L - k_\eta}{\log(k_L) - \log(k_\eta)}.$$

(16)

This yields the eddy–viscosity:

$$\nu_\tau = \alpha^2 \Delta^2 \left(\frac{\psi}{\psi + e^{k_c}}\right) \left|\overline{\overline{\mathcal{S}}}\right|.$$

(17)

Given this form of the eddy–viscosity, $\nu_\tau \to 0$ as $\overline{\Delta} \to 0$. To ensure the asymptotic behaviour in high shear regions, it is necessary to couple the new formulation of the eddy–viscosity with mesh adaptivity, such that $\Delta \to \eta$ in those regions. The next section explains how the anisotropic mesh adaptivity method is implemented.

3.2. Anisotropic mesh adaptivity

Mesh adaptivity allows the mesh resolution to change dynamically based on flow features. Resolution can thus be increased locally to represent complex flows at small length scales without refining the whole spatial domain.

Pain et al. [45] developed a mesh adaptivity process guided by a metric, $\mathcal{M}$, that includes information about a solution field χ through its Hessian $\mathcal{H} \equiv \nabla^T \nabla \chi$. This metric $\mathcal{M}$ is derived from an interpolation error ϵ:

$$\epsilon = \Delta_{ij}^2 \left|\mathcal{H}^e\right|,$$

(18)

where Δ_{ij}^2 is a diagonal matrix with element lengths in all directions, and $|\mathcal{H}^e|$ is a normalised Hessian of the solution field χ on element e. This normalised Hessian is defined as:

$$\left|\mathcal{H}^e\right| = \frac{\mathcal{H}^e}{\max\{|\chi|, \chi_{\min}\}}.$$

(19)

The metric $\mathcal{M}$ is defined such that the element has unit size with respect to $\mathcal{M}$ for a specified interpolation error ϵ:

$$\mathcal{M} = \frac{|\mathcal{H}^e|}{\epsilon}.$$

(20)

This metric is a symmetric positive–definite matrix and can be decomposed into eigenvalues and eigenvectors:

$$\mathcal{M} = \mathbf{V} \Lambda \mathbf{V^T} = \mathbf{V} \begin{bmatrix} \lambda_\xi & 0 & 0 \\ 0 & \lambda_\eta & 0 \\ 0 & 0 & \lambda_\zeta \end{bmatrix} \mathbf{V^T},$$
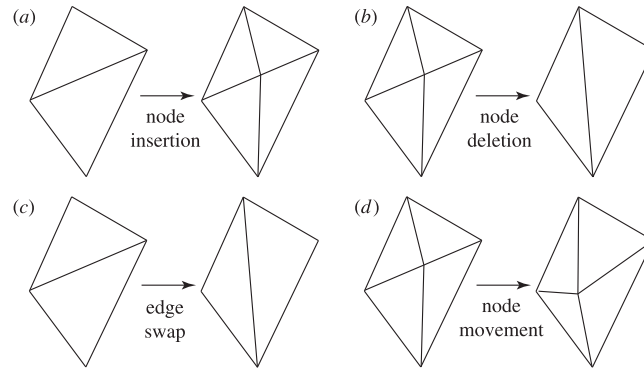
(21)

9

Fig. 7. Example of mesh modification operations in 2D: (a) node insertion or edge split, (b) node deletion or edge collapse,(c) edge swap and (d) node movement [46].

where $\mathbf{V}$ is an orthonormal matrix of eigenvectors and Λ a diagonal matrix of eigenvalues. $\mathbf{V}$ and Λ are thus rotation and scaling matrices respectively. Hence, the metric can be considered a transformation matrix from the metric space (ξ, η, ζ) to a physical space (x, y, z). The eigenvalues λ_i relate to element size by:

$$\lambda_i = \Delta_i^{-2}. \tag{22}$$

Given the desired element size, defined by the metric $\mathcal{M}$, an optimisation–based adaptivity algorithm seeks to improve mesh quality by performing topological operations [46] (see Fig. 7). In 2D these operations include

(a) node insertion or edge splitting,
(b) node deletion or edge collapse,
(c) edge swapping and
(d) node movement.

In 3D face-edge swapping is also possible. The node insertion or edge splitting corresponds to mesh refinement, increasing the number of degrees of freedom. In contrast, node deletion or edge collapse corresponds to mesh coarsening, reducing the number of degrees of freedom. Edge–edge and edge–face swapping as well as node movement operations do not affect the total number of degrees of freedom and are intended to improve a quality measure for the elements.

Regardless of the element anisotropy handled by the mesh adaptivity process, the form of eddy–viscosity in Eq. (17) constrains it to an isotropic approach, where the filter width $\overline{\Delta} = \alpha A^{1/2}$, with A being the area of the element in 2D, and $\overline{\Delta} = \alpha V^{1/3}$, with V being the volume of the element in 3D. Therefore, a tensorial formulation of Eq. (17) is required to properly account for anisotropy in eddy–viscosity.

3.3. Tensorial formulation of the eddy–viscosity

The scalar quantity produced by the formulation of the eddy–viscosity from Eq. (17) can be incorporated into the filtered Navier–Stokes equation as an isotropic viscosity. This formulation does not properly account for anisotropic filtering as it has the same effect in all directions. Therefore, a formulation of the eddy–viscosity that accounts for anisotropy is required. Recalling equation (10), the tensorial formulation of the filter width takes advantage of the metric $\mathcal{M}$ as defined by Pain et al. [45], being related to the metric by:

$$\overline{\Delta}_{ij}^2 = \mathbf{V}^{\mathbf{T}} \begin{bmatrix} \overline{\Delta}_{\xi}^2 & 0 & 0 \\ 0 & \overline{\Delta}_{\eta}^2 & 0 \\ 0 & 0 & \overline{\Delta}_{\zeta}^2 \end{bmatrix} \mathbf{V} = \mathbf{V}^{\mathbf{T}} \begin{bmatrix} \alpha^2 \lambda_{\xi}^{-1} & 0 & 0 \\ 0 & \alpha^2 \lambda_{\eta}^{-1} & 0 \\ 0 & 0 & \alpha^2 \lambda_{\zeta}^{-1} \end{bmatrix} \mathbf{V} = \alpha^2 \mathcal{M}^{-1}. \tag{23}$$

Using the tensorial form of the filter width, equation (17) can be rewritten in tensor form as:

$$\overline{\overline{\nu}}_{\tau} = \alpha^2 \left| \overline{\overline{\mathcal{S}}} \right| \Delta_{ij}^2 \left(\psi \mathbf{I} \left(\psi \mathbf{I} + \exp(k_{cij}) \right)^{-1} \right), \tag{24}$$

where $k_{cij} = \pi \overline{\Delta}_{ij}^{-1}$ is the tensorial form of the cut–off filter wavenumber. This can be written in terms of the metric $\mathcal{M} = \mathbf{V^T} \Lambda \mathbf{V}$ as:

$$k_{cij} = \mathbf{V} \begin{bmatrix} \pi\alpha^{-1}\lambda_\xi^{1/2} & 0 & 0 \\ 0 & \pi\alpha^{-1}\lambda_\eta^{1/2} & 0 \\ 0 & 0 & \pi\alpha^{-1}\lambda_\zeta^{1/2} \end{bmatrix} \mathbf{V^T} = \frac{\pi}{\alpha}\mathbf{V}\Lambda^{1/2}\mathbf{V^T} = \frac{\pi}{\alpha}\mathcal{M}^{1/2}, \tag{25}$$

hence, equation (24) becomes:

$$\overline{\overline{v}}_\tau = \alpha^2 \left|\overline{\overline{\mathcal{S}}}\right| \mathcal{M}^{-1}\left(\psi\mathbf{I}\left(\psi\mathbf{I} + \frac{\pi}{\alpha}\exp(\mathcal{M}^{1/2})\right)^{-1}\right). \tag{26}$$

Since $\mathcal{M}$ is symmetric positive–definite, equation (26) can be further simplified as:

$$\overline{\overline{v}}_\tau = \alpha^2 \left|\overline{\overline{\mathcal{S}}}\right| \mathcal{L}, \tag{27}$$

with $\mathcal{L} = \mathbf{V^T}\Lambda^{-1}\Phi^\star\mathbf{V}$, and

$$\Phi^\star = \psi\mathbf{I}\left(\psi\mathbf{I} + \frac{\pi}{\alpha}\exp(\Lambda^{1/2})\right)^{-1}. \tag{28}$$

Here $\Phi^\star$ is a diagonal matrix, with non–zero entries:

$$\Phi_{ii}^\star = \frac{\psi}{\left(\psi + \frac{\pi}{\alpha}\exp(\lambda_{ii}^{1/2})\right)}. \tag{29}$$

Given the tensorial form of the eddy–viscosity, the mesh adaptivity method is aimed at refining high shear regions in relevant directions and coarsening those regions with low turbulence fluctuations through analysis of flow topology.

3.4. Flow topology

To identify high shear regions and low turbulence fluctuations regions, the velocity gradient tensor $\nabla\mathbf{u}$ is used. This tensor is related to the topology of the flow through its invariants [47,48]. The velocity gradient tensor can be decomposed into a symmetric and a skew–symmetric component:

$$\nabla\mathbf{u} = \frac{1}{2}(\nabla\mathbf{u} + \nabla\mathbf{u}^T) + \frac{1}{2}(\nabla\mathbf{u} - \nabla\mathbf{u}^T) = \overline{\overline{\mathcal{S}}} + \overline{\overline{\Omega}}, \tag{30}$$

where the symmetric component $\overline{\overline{\mathcal{S}}}$ is the strain–rate tensor, and the skew–symmetric component $\overline{\overline{\Omega}}$ is the rotation–rate tensor.

The invariants of velocity gradient tensor are defined as the coefficients of its characteristic equation:

$$\lambda^3 + P\lambda^2 + Q\lambda + R = 0. \tag{31}$$

The invariants P, Q and R are:

$$P = -\sum_i \nabla\mathbf{u}_{ii}, \tag{32}$$

$$Q = \frac{1}{2}\left(\left\|\overline{\overline{\Omega}}\right\|_F^2 - \left\|\overline{\overline{\mathcal{S}}}\right\|_F^2\right), \tag{33}$$

$$R = -\det(\nabla\mathbf{u}), \tag{34}$$

where $\|\cdot\|_F$ is the Frobenius norm.

For incompressible fluids $P = -\nabla\mathbf{u} = 0$, therefore the flow topology depends only on the second (Q) and third (R) invariants. The second invariant Q is widely used as a vortex identification method, known as the Q criterion [49] which assumes that $Q > 0$ implies an excess of local rotation with respect to local strain. However, both terms involved in calculating Q contain a part of the total shear, hence, Q can be positive due to the amount of
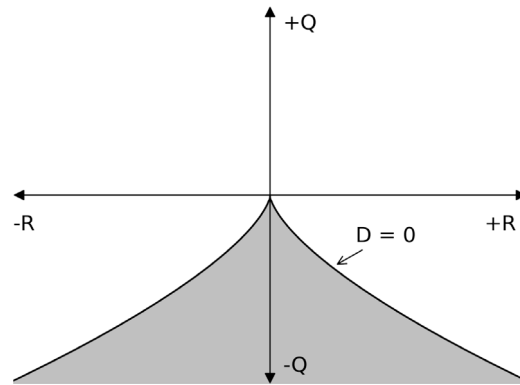
Fig. 8. Q–R space showing the real solutions region, corresponding to non–rotating dissipative flow (shaded) and the complex solutions region corresponding to rotating flow.

shear in either $\overline{\overline{\mathcal{S}}}$ or $\overline{\overline{\Omega}}$ rather than due to excess of rotation. This can be inferred from the work of Chong et al. [47] that describes flow topology based on local solutions of the characteristic polynomial of the velocity gradient tensor (Eq (31)) in the P–Q–R space. Given the condition $P = 0$, the solutions to this equation lie in the plane $P = 0$ of the P–Q–R space, and can be real or complex. The type of solution is determined by the discriminant:

$$D = 4Q^3 + 27R^2. \tag{35}$$

The case $D = 0$, defines the curve that separates the region of real solutions, related to non–rotating dissipative flow, from the region of complex solutions, related to rotating flow. If $D < 0$ all solutions are real, if $D > 0$ there is one real solution and conjugate complex solutions. This is illustrated in Fig. 8.

Further analysis of the Q–R space allows specific patterns in the flow topology to be identified as different regions bounded by the discriminant D and the line $R = 0$, as explained by da Silva and Pereira [50]. The topology patterns are: vortex stretching, vortex compression, strain stretching and compression. Fig. 9 displays the topology patterns regions and the boundary lines. These boundary lines define the topology boundary layers. A special case is the $R = 0$ line, that could either mean a boundary layer or a no–flow/steady–flow condition.
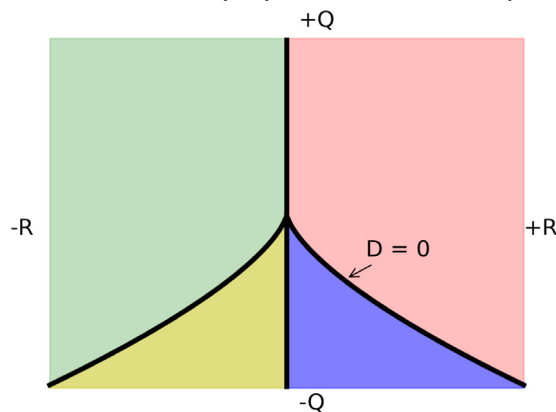

Fig. 9. Q–R space showing the different topology patterns zones: vortex stretching (green), vortex compression (red), strain stretching (yellow) and strain compression (blue). The black lines define the topologies boundary layers or no–flow condition. (For interpretation of the references to colour in this figure legend, the reader is referred to the web version of this article.)

Given this classification of the flow topology in Q–R plane, the lines $D = 0$ and $R = 0$ define boundary layers between flow patterns in unsteady fluid flow, thus these lines can be used to identify high shear regions in the

physical domain. This can be carried out by defining scalar fields $D^\star$ and $R^\star$:

$$
D^\star = \begin{cases} -1 & \text{if } D < -\varepsilon_D, \\ 0 & \text{if } -\varepsilon_D < D < \varepsilon_D, \\ 1 & \text{if } D > \varepsilon_D, \end{cases} \tag{36}
$$

$$
R^\star = \begin{cases} -1 & \text{if } R < -\varepsilon_R, \\ 0 & \text{if } -\varepsilon_R < R < \varepsilon_R, \\ 1 & \text{if } R > \varepsilon_R, \end{cases} \tag{37}
$$

where ε_D and ε_R are small numbers to define a threshold for boundary layers identification. $D^\star$ allows for the identification of boundary layers due to rotating and non–rotating fluid interactions, whilst $R^\star$ allows for the identification of boundary layers due to interactions between vortices and due to no–slip interactions with physical boundaries. These scalar fields are used to drive mesh adaptivity given that gradients of these fields are only present in the vicinity of $D = 0$ and $R = 0$.

Now that we have established the way to identify high shear regions, the aim is to minimise eddy–viscosity in these regions. This is achieved by refining high shear regions such that the filter width, as a function of the element size, is closer to the Kolmogorov scale, and consequently the eddy–viscosity approaches zero in these regions. The Kolmogorov scale can be calculated by recalling that it is the length scale at which the Reynolds number is locally minimised to 1, i.e. $Re_\Delta \to 1$ if $\Delta \to \eta$. In contrast, low shear regions are coarsened and the subgrid–scale model is applied locally in those regions, modelling the flow in those elements at larger turbulence scales.

The level of mesh refinement can be constrained using a minimum edge length parameter (m). This parameter is intended to avoid over refinement that would make simulations prohibitively expensive. In the new model implementation, this parameter can be defined as the Kolmogorov scale η, that would lead to DNS. However, the minimum edge length can be defined as $\max\{m, \eta\}$ to avoid undesired over refinement.

The procedure is summarised in algorithm 1:

Algorithm 1: Procedure for parameter–free turbulence model for mesh adaptivity

    Input : L integral length scale
    Input : m minimum element size allowed
    if *in adaptive timestep* **then**
        Calculate Kolmogorov scale η
        Define minimum element size: $\max\{m, \eta\}$
        Calculate $D^\star$ (Eq. (36)) and $R^\star$ (Eq. (37))
        Run adaptivity algorithm for fields $R^\star$ and $D^\star$
    end
    Calculate eddy–viscosity ν_τ (Eq. (27))
    Solve filtered equations (Eq. (3))

The model presented in this algorithm implicitly implements the two strategies for overcoming the diffusive behaviour of the Smagorinsky model shown in Fig. 5:

  (*i*) local refinement in the high shear regions, including but not limited to near–wall regions, and
  (*ii*) a modified formulation of the eddy–viscosity, accounting for anisotropy.

Therefore, this turbulence model results in a satisfactory wall model, refining appropriately velocity boundary layers. This model is also suitable for temperature boundary layers.

For laminar flow over a wall, velocity and temperature boundary layers are related by:

$$
Pr^{-1/3} = \frac{\delta_T}{\delta_u}, \tag{38}
$$

where $Pr = \nu/\alpha$ is the Prandtl number of the fluid, with ν and α the kinematic viscosity and the thermal diffusivity of the fluid, δ_T is the thickness of the temperature layer and δ_u the thickness of the velocity layer. Given this relation, for fluids with $Pr \sim 1$ both boundary layers have similar thickness, thus the refinement for the velocity boundary

layer is appropriate for the temperature layers. The assumption of similar boundary layer thickness is valid for most gases, with $Pr \approx 0.7$.

For turbulent flow over a wall, heat transport is mainly driven by the velocity field, therefore both boundary layers are defined by the velocity fluctuations. This leads to the assumption $\delta_T \approx \delta_u$. Therefore, the mesh adaptivity process driven by flow topology as presented in this new turbulence model is appropriate for solving the temperature field in coupled fluid flow–heat transfer problems without the need to use an error measure for temperature and an adapt of the mesh explicitly taking account of the temperature field.

4. Model testing

For this work, the code used for the numerical solution of the governing equations is the CFD code Fluidity [51, 52] developed by the Applied Modelling & Computation Group (AMCG) at Imperial College London.

The model presented in this work was tested using a flow past a sphere test case. This test case is well documented in the literature for both experimental and numerical studies, which allows the performance of the new model to be assessed. The results obtained with the new model were compared both quantitatively and qualitatively to results obtained with the standard Smagorinsky model implemented in Fluidity, and demonstrated the better performance of this new method at lower computational cost. The reduced computational cost enabled larger Reynolds number simulations to be carried out, obtaining good results at reasonable computational cost.

Quantitative assessment was carried out by comparing the time–averaged velocity in the wake behind the sphere and the drag coefficient, C_D, obtained from previous studies and the value calculated using the results obtained using the new model. For these comparisons both experimental results and standard empirical relationships were used. Additionally, the results obtained with the standard Smagorinsky model and results from DNS reported in the literature were included in these comparisons to assess the accuracy of the new model with respect to other numerical approximations. The drag coefficient is calculated as [53]:

$$C_D = \frac{2F_D}{\rho u_0^2 A}, \tag{39}$$

where F_D is the force applied by the fluid stream on the surface of the sphere, ρ is the fluid density, u_0 is the inflow velocity and A is the cross–sectional area of the sphere.

Qualitative assessment was carried out by visually comparing the wake behind the sphere and the ability of the numerical approximations to represent eddy structures in the wake. For this comparison DNS results available in the literature were used as reference, as these simulations have the highest spatial resolution.

The computational domain consists of a sphere of diameter $d = 1$ centred at point $(0, 0, 0)$, bounded by a box centred at point $(5d, 0, 0)$, with the distance between the parallel planes: top–bottom $20d$, front–back $20d$ and left–right $30d$. A constant velocity $\mathbf{u} = [1, 0, 0]^T$ was prescribed on the left boundary. The boundary condition for the top, bottom, front and back boundaries was $\mathbf{u} \cdot \hat{\mathbf{n}} = 0$, characteristic of an impermeable wall. The domain was discretised into an unstructured tetrahedral mesh, with initial edge lengths of 0.05 on the surface of the sphere and edge lengths of 1 elsewhere. This is shown in Fig. 10.

The tests were carried out for different Reynolds numbers ranging from $Re = 10^3$ to $Re = 10^6$. Given the change in the complexity of the flow over this range of Reynolds numbers, the simulation time was defined to allow for fully developed flow to be attained. Fig. 11 shows the time–averaged stream–wise velocity $\langle u_x \rangle$ in the wake behind the sphere over the midline $y = 0$, $z = 0$. This figure displays data from experimental studies [54], and DNS results [55–58]. Fig. 12 shows the drag coefficient as a function of Reynolds number for the flow past a sphere test case. This figure displays data from experimental studies [59–61], empirical relationships based on experimental data [62–65] and results from a high resolution (over 130×10^6 nodes) numerical approximation [66]. For the simulations using Fluidity, a maximum number of nodes of 5×10^6 was initially specified for mesh adaptivity. Mesh adaptivity was applied for the Smagorinsky model using the velocity field for the metric calculation (Eq. (20)). The simulations using the new model follow the procedure shown in algorithm 1.

Time–averaged stream–wise velocity results show good agreement compared to the reference studies for both Smagorinsky model and the new model. However, for the cases shown in Fig. 11 the results obtained with the new model are consistently more accurate, compared to the results obtained using the Smagorinsky model. This is particularly noticeable in the case $Re = 2 \times 10^4$, where the results obtained using the Smagorinsky model differ
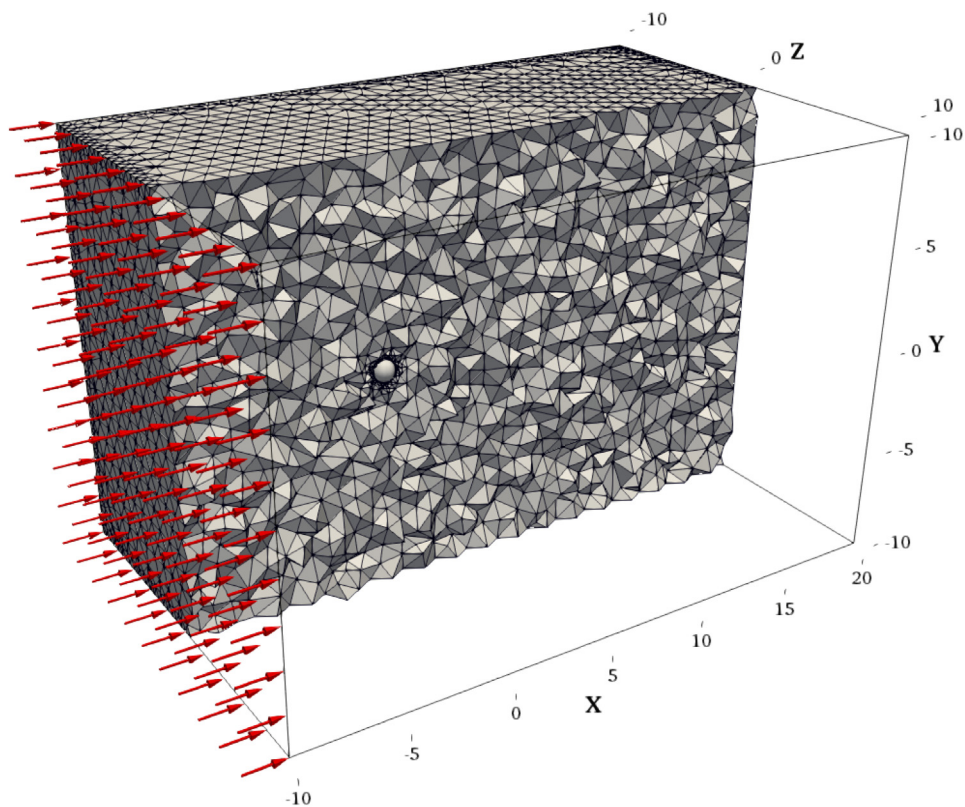
(a) Computational domain
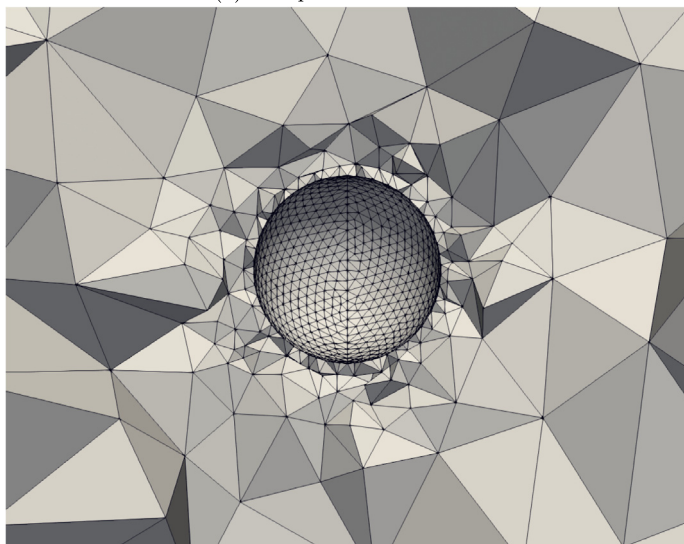
(b) Sphere discretisation

Fig. 10. Computational domain for the flow past a sphere test case, the initial mesh shown is composed of approximately 25,000 nodes and 130,000 elements.(a) longitudinal section at $z = 0$ with a prescribed velocity field on left boundary (red glyphs). (b) zoom–in sphere region. (For interpretation of the references to colour in this figure legend, the reader is referred to the web version of this article.)

(a) $Re = 1000$

(b) $Re = 3700$

(c) $Re = 20000$

Fig. 11. Time–averaged stream–wise velocity $\langle u_x \rangle$ on the wake of the flow behind the sphere over the midline $y = 0$, $z = 0$, at different Reynolds numbers.

Fig. 12. Comparison of the drag coefficient C_D on the sphere surface. Experimental data from [59–61]. Empirical relationships from [62–65]. Numerical solutions from [66] and those calculated with Fluidity using the Smagorinsky model and the new model developed in this work.

from the reference study [55] in the region near the sphere, whilst the results obtained using the new model follow the results from the reference study.

The new model is able to capture the drag coefficient behaviour over the simulated Reynolds number range (from $Re = 10^3$ to $Re = 10^6$), particularly for the so–called drag crisis, where the drag coefficient decreases dramatically at approximately $Re > 2 \times 10^5$, reaching a minimum value between $Re = 3 \times 10^5$ and $Re = 5 \times 10^5$ before increasing again. This phenomenon has been observed experimentally, however, it is difficult to calculate the error in the numerical approximations with respect to experimental results given the differences in experimental studies. The results obtained with the new model are also compared to other numerical results such as those of Geier et al. [66] as shown in Fig. 12. In that work they used the lattice–Boltzmann method with non–uniform grids of 40×10^6, 74×10^6 and 133×10^6 nodes. Those grids were locally refined to have maximum resolution in the regions around and behind the sphere. In their work, only the simulations performed with the highest resolution were able to capture the drag crisis within a Reynolds number range from $Re = 2 \times 10^5$ to $Re = 10^6$. Simulations in Fluidity using the Smagorinsky model show good agreement to previous studies and captures the drag crisis up to $Re = 3 \times 10^5$. Therefore there is no significant difference between the new model and the Smagorinsky model in terms of accuracy for calculating the drag coefficient within this Reynolds number range. However, the Smagorinsky model fails to capture the drag coefficient increase beyond $Re = 3 \times 10^5$, thus results using Smagorinsky model are not consistent with other studies for larger Reynolds numbers. This result is an effect of the resolution limitation introduced to these simulations in terms of maximum number of nodes (5×10^6). The same simulation without limiting the number of nodes was able to capture drag coefficient consistently for $Re = 5 \times 10^5$ and $Re = 1 \times 10^6$, by allowing the number of nodes to increase up to 14×10^6. Fig. 13 shows the maximum number of nodes in Fluidity simulations using the Smagorinsky model and the new model.
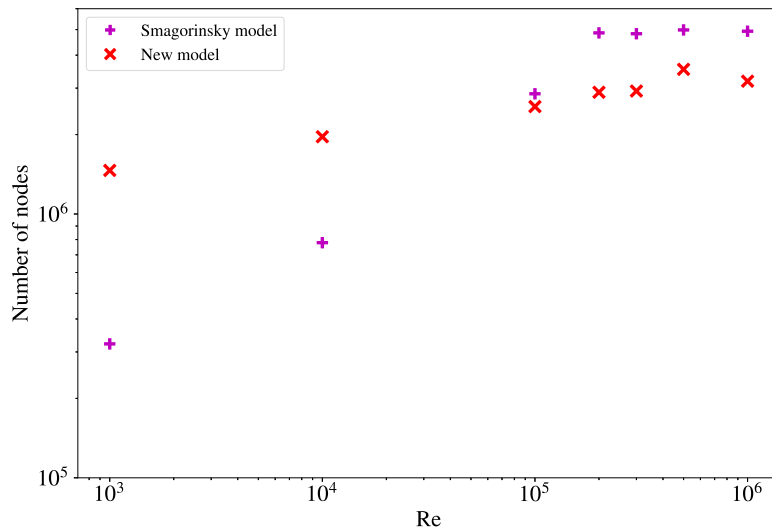

Fig. 13. Comparison of the number of nodes in the adapted meshes for Fluidity simulations using the Smagorinsky model and the new model developed in this work.

Considering that the new model introduces additional calculations compared to the Smagorinsky model, particularly in those timesteps when adaptivity occurs, it is important to quantify the effect of these additional calculations on the computational cost. The ratio of the simulation time per timestep to the number of nodes was used for this assessment. From these calculations, it was found that for the Smagorinsky model this ratio ranges from 2.34×10^{-4} to 3.95×10^{-4} seconds per node in mesh adaptivity timesteps, whilst for the new model this ratio ranges from 4.13×10^{-4} to 8.1×10^{-4} seconds per node in mesh adaptivity timesteps. Regardless of the increased time per node ratio in the new model, the computational cost of the new model at higher Reynolds number is significantly smaller compared to the Smagorinsky model, given the reduced number of nodes.

For the lower Reynolds number range ($Re = 10^3$ and $Re = 10^4$) there is no advantage in using the new model relative to the Smagorinsky model in terms of accuracy, as seen in Fig. 12, and in terms of computational cost, as seen in Fig. 13 given that the maximum number of nodes for the simulations using the new model is greater

than the number of nodes using the Smagorinsky model. However, a qualitative assessment of the wake behind the sphere shows a better performance of the new model compared to the Smagorinsky model. This assessment was carried out using the vortex identification method proposed by Liu et al. [67]. This method looks for regions in the domain where vorticity overtakes deformation, based on the components of the velocity gradient tensor ($\overline{\overline{S}}$ and $\overline{\overline{\Omega}}$) and introducing the ratio:

$$\omega = \frac{\left\|\overline{\overline{\Omega}}\right\|_F^2}{\left\|\overline{\overline{S}}\right\|_F^2 + \left\|\overline{\overline{\Omega}}\right\|_F^2 + \varepsilon}, \tag{40}$$

where ε is a small number used to avoid division by zero. Using this method, eddy structures can be visualised as an iso–surface $\omega > 0.5$. Fig. 14 shows the wake behind the sphere for simulations using the Smagorinsky model and the new model with the iso–surface $\omega = 0.51$.

From Fig. 14 it can be observed that the new turbulence model is able to better resolve eddy structures which the Smagorinsky model fails to capture. This lower performance of the Smagorinsky model can be identified as a coarser representation of the wake compared to the new model result. This is due to refinement not specifically being carried out in the boundary layer region as mesh adaptivity is driven by the velocity field. This establishes an advantage of the new model compared to the Smagorinsky model for Reynolds numbers up to $Re = 1 \times 10^5$, where the new model requires more nodes than the Smagorinsky model.

A new method for vortex identification can be defined based on the physical meaning of the Q–R space shown in Fig. 9 by looking for the boundary layers given by the regions in the domain where $D^\star = 0$ or $R^\star = 0$. Fig. 15 shows the flow wake behind the sphere using the $D^\star - R^\star$ criterion introduced with the new model for the case $Re = 1000$.

This new vortex identification method captures additional eddy structures in the wake, which were not detected by the omega method defined by Liu et al. [67]. These additional eddy structures can be observed in the DNS results [68,69], therefore, the new vortex identification method succeeds in identifying eddy structures that other vortex identification methods only describe at DNS resolutions. However, this new vortex identification method can be sensitive to the threshold defined by ε_D and ε_R. Fig. 16 shows the wake for $Re = 1000$ using a larger threshold where small eddy structures close to each other are merged into larger eddy structures due to an over estimation of the boundary layer defining vortex sheets or tubes.

This new vortex identification method is also used to visualise the flow wake for a number of increasing Reynolds number cases. Figs. 17 and 18 show the flow wake for $Re = 10^4$ and $Re = 10^6$, respectively, alongside some of the results from previous studies [66,70,71] for comparison purposes.

These results can be compared to experimental results by Taneda [71] in terms of the location of the separation layer on the sphere surface. This separation layer moves to the back hemisphere as seen for the case $Re = 10^6$ (Fig. 18(a)) compared to lower Reynolds numbers, leading to the formation of smaller vortex structures detaching from the sphere surface, as the Reynolds number increases. A more detailed comparison of the structures detaching from the sphere surface can be performed by comparing these results to higher resolution numerical results by Rodríguez et al. [72], Geier et al. [69], Geier et al. [66] and Nagata et al. [68]. The results obtained using the new model are consistent with those presented in the cited studies, capturing large and small scale structures despite the lower overall resolution used in this work. Additionally, vortex shedding patterns obtained with the new model are consistent with both experimental and numerical studies found in the literature.

The capability of the new turbulence model to capture eddy structures of different length scales demonstrates the complementary effect of the implicit turbulence scales separation carried out by the parameter–free eddy viscosity formulation and anisotropic mesh adaptivity driven by flow topology.

5. Conclusions & future work

A new, parameter–free turbulence model for anisotropic mesh adaptivity has been developed and tested using the flow past a sphere case. This model incorporates an implicit length scale, based not only on the local element size but also on the local turbulence scale. This formulation of the length scale allows for an asymptotic behaviour of the eddy–viscosity with respect to local turbulent perturbations. This formulation of the eddy viscosity has been coupled with the anisotropic mesh adaptivity algorithm implemented in Fluidity, defining a new criterion for identifying high
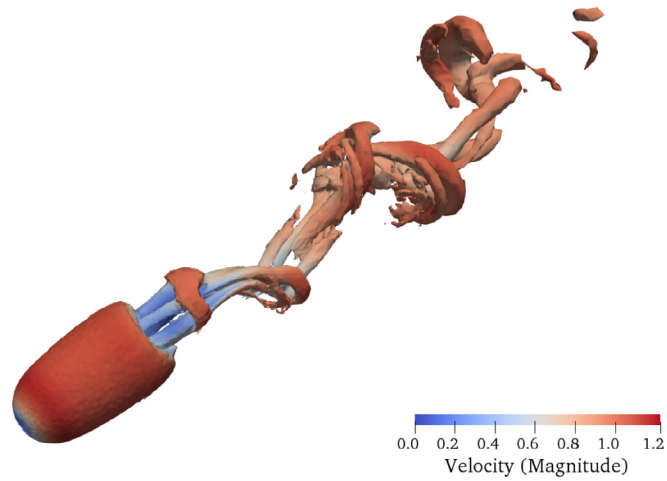
(a) Iso–surface $\omega = 0.51$ using the Smagorinsky model for the case $Re = 1000$ (maximum number of nodes: 0.322×10^6)
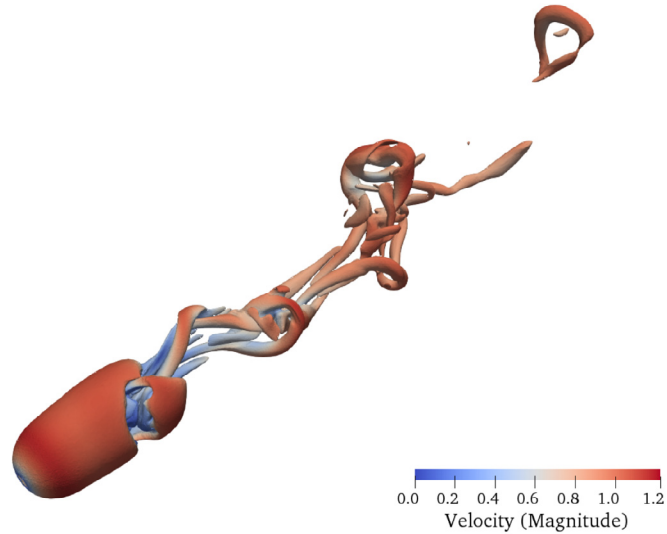
(b) Iso–surface $\omega = 0.51$ using the new model for the case $Re = 1000$ (maximum number of nodes: 1.463×10^6)
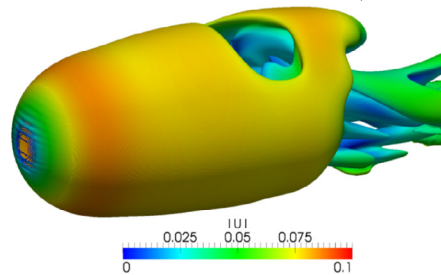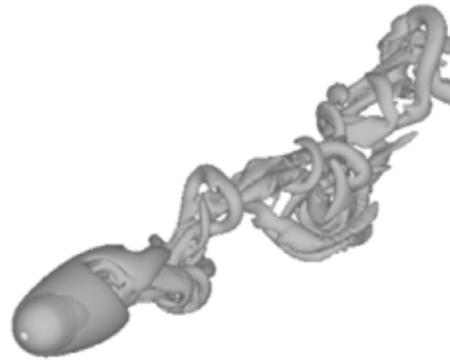

(c) Visualisation of eddy structures close to the sphere for the case $Re = 1000$ using 27×10^6 nodes (from [68], included with the permission of the publishers).

Fig. 14. Flow wake behind a sphere for $Re = 1000$, coloured by velocity magnitude, using (a)the Smagorinsky model and (b) the new model. (c) Shows the result from a previous DNS study for comparison purposes. The Smagorinsky model is able to capture larger eddy structures, however smaller structures can only be visualised from the results using the new model. Additionally, a better visualisation of the eddy structures can be achieved with the new model, when comparing the iso–surfaces in (a) and (b) to the DNS result in (c).
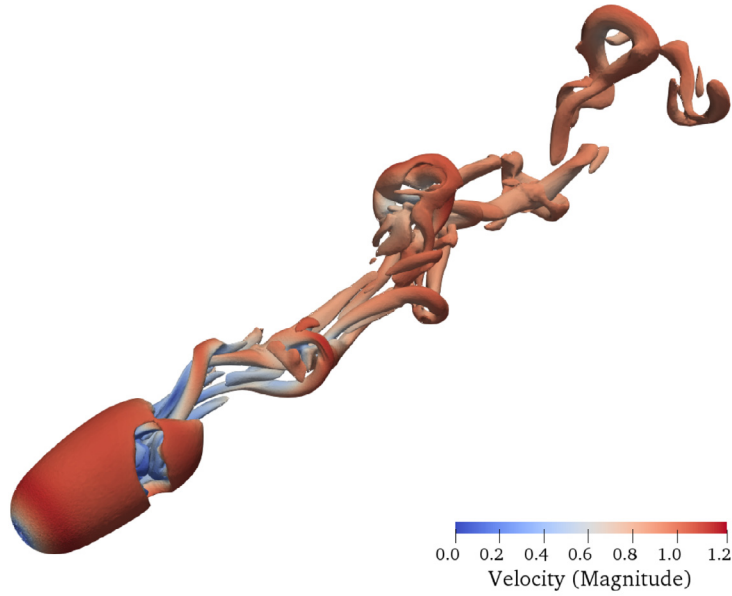
(a) Flow wake behind the sphere using the $D^\star - R^\star$ criterion introduced with the new model for the case $Re = 1000$ (maximum number of nodes: 1.463×10^6).

(b) Flow wake behind the sphere for the case $Re = 1000$ using 15×10^6 nodes (from [69], included with the permission of the publishers).

Fig. 15. Visualisation of the flow wake behind a sphere for $Re = 1000$ (a) using the $D^\star - R^\star$ criterion and (b) using the second invariant of velocity gradient tensor ($Q/u_\infty^2 = 5.0 \times 10^{-4}$) and DNS (included for comparison purposes). The $D^\star - R^\star$ criterion achieves to identify more eddy structures than the omega method (Fig. 14(b)), some of them only identifiable at DNS resolution.

shear regions. This criterion is based on flow topology by mapping the local flow conditions into the velocity gradient tensor invariants space $P-Q-R$. This mapping for driving mesh adaptivity demonstrated an improved performance in terms of computational cost by focusing mesh refinement in the regions of interest defined by $D^\star$ and $R^\star$, resulting in a reduced number of nodes at high Reynolds numbers compared to mesh adaptivity driven by the velocity field and using the Smagorinsky model for turbulence. For Reynolds numbers up to $Re = 10^5$, the Smagorinsky model is computationally cheaper than the new model, however, the new model performs better in terms of its capability for describing the flow wake behind the sphere. For $Re > 10^5$ the accuracy of the new turbulence model has been demonstrated by its capability in capturing the drag crisis phenomenon where the Smagorinsky model fails and obtaining results which are consistent with both experimental data and higher resolutions numerical results.
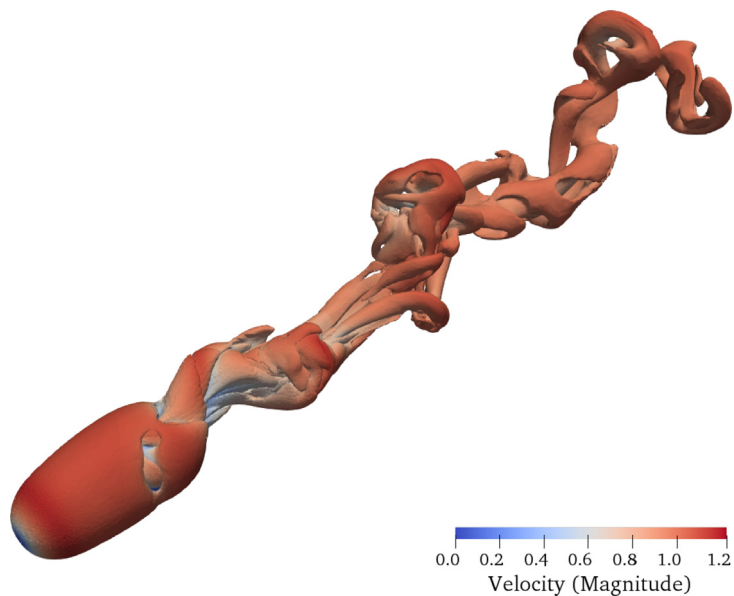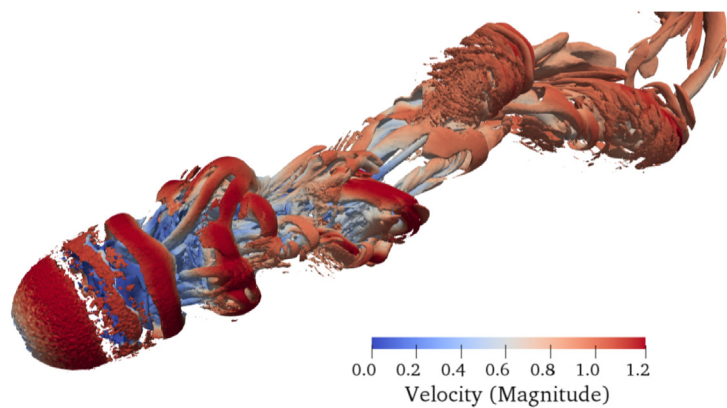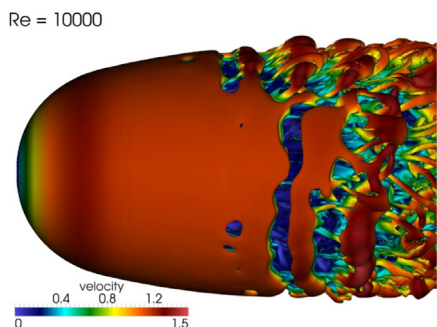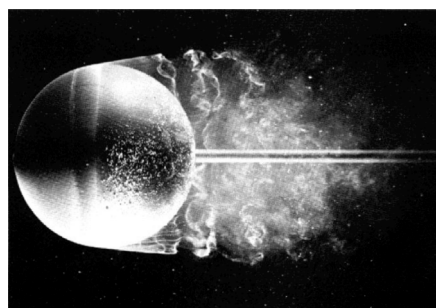
Fig. 16. Flow wake behind the sphere using the $D^\star - R^\star$ criterion introduced with the new model for the case $Re = 1000$ with a larger threshold, resulting in a less detailed description of smaller eddy structures.
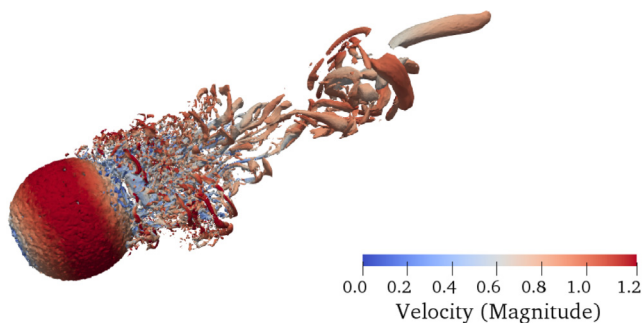

(a) Flow wake for $Re = 10^4$

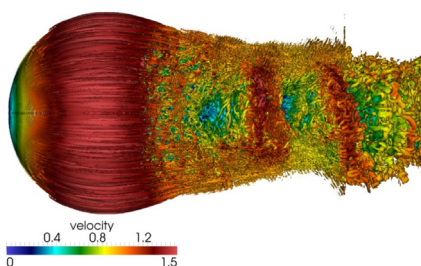(b) Visualisation of eddy structures close to the sphere for $Re = 10^4$ (from [66]).

(c) Visualisation of eddy structures close to the sphere for $Re = 1.5 \times 10^4$ (from [70]).

Fig. 17. Flow wake behind the sphere using the $D^\star - R^\star$ criterion for (a) $Re = 10^4$, (b) $Re = 2 \times 10^5$ and (c) $Re = 10^6$.
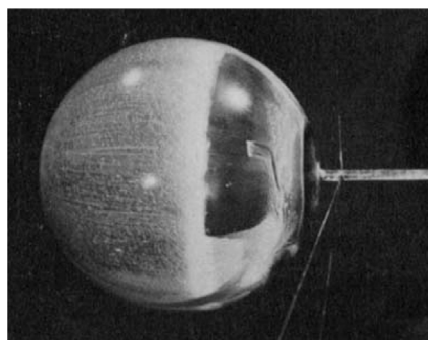
(a) Flow wake for $Re = 10^6$

(b) Visualisation of eddy structures close to the sphere for $Re = 1.14 \times 10^6$ (from [66]).

(c) Visualisation of the flow separation layer for $Re = 0.95 \times 10^6$ using the oil–flow method (from [71]).

Fig. 18. Flow wake behind the sphere using the $D^\star - R^\star$ criterion for (a) $Re = 10^4$, (b) $Re = 2 \times 10^5$ and (c) $Re = 10^6$.

The new turbulence model presented in this article succeeds in describing the flow wake behind the sphere for the different Reynolds numbers simulated, taking advantage of anisotropic mesh adaptivity. The results obtained are broadly comparable with DNS results, at a much lower computational cost. Therefore, this new turbulence model provides an alternative that balances computational cost and accuracy.

The ability of the new model to accurately describe eddies is particularly advantageous for heat and mass transport applications, considering their relevance for advection. Moreover, the new model is capable of handling different turbulence scales, making it appropriate for applications involving a wide range of length scales, at a reasonable cost.

Future focus for this work includes the implementation and validation of the new model for multiphase flow and coupled fluids–heat transfer problems. This would extend the capabilities of the model to a wider range of applications. Additionally, the definition of the boundary layer threshold and the analysis of the physical and numerical effects of it on the model performance will be a matter of future studies.

Declaration of competing interest

Data availability

Data will be made available on request.

Acknowledgements

References

[1] P. Moin, K. Mahesh, Direct numerical simulation: A tool in turbulence research, Annu. Rev. Fluid Mech. 30 (1) (1998) 539–578.

[2] M. Breuer, N. Jovičić, K. Mazaev, Comparison of DES, RANS and LES for the separated flow around a flat plate at high incidence, Int. J. Num. Methods fluids 41 (4) (2003) 357–388.

[3] S. Lardeau, M.A. Leschziner, Unsteady RANS modelling of wake–blade interaction: Computational requirements and limitations, Comput. & Fluids 34 (1) (2005) 3–21, URL https://www.sciencedirect.com/science/article/pii/S0045793004000581.

[4] K. Hanjalic, Will RANS Survive LES? A View of Perspectives, J. Fluids Eng. 127 (5) (2005) 831–839, http://dx.doi.org/10.1115/1.2037084, arXiv:https://asmedigitalcollection.asme.org/fluidsengineering/article-pdf/127/5/831/5835007/831_1.pdf.

[5] R. Schwarze, F. Obermeier, Performance and limitations of the unsteady RANS approach, PAMM 6 (1) (2006) 543–544, URL https://onlinelibrary.wiley.com/doi/abs/10.1002/pamm.200610252.

[6] S.B. Pope, Turbulent Flows, Cambridge University Press, 2000.

[7] H. Choi, P. Moin, Grid-point requirements for large eddy simulation: Chapman's estimates revisited, Phys. Fluids 24 (1) (2012) 011702, http://dx.doi.org/10.1063/1.3676783.

[8] U. Piomelli, Large-eddy simulation: Achievements and challenges, Prog. Aerosp. Sci. 35 (4) (1999) 335–362, URL https://www.sciencedirect.com/science/article/pii/S0376042198000141.

[9] M. Lesieur, O. Metais, New trends in large-eddy simulations of turbulence, Annu. Rev. Fluid Mech. 28 (1) (1996) 45–82.

[10] R. Maulik, O. San, Explicit and implicit LES closures for Burgers turbulence, J. Comput. Appl. Math. 327 (2018) 12–40, URL https://www.sciencedirect.com/science/article/pii/S0377042717303035.

[11] S.B. Pope, Ten questions concerning the large-eddy simulation of turbulent flows, New J. Phys. 6 (1) (2004) 35.

[12] Y. Zhiyin, Large-eddy simulation: Past, present and the future, Chin. J. Aeronaut. 28 (1) (2015) 11–24, URL https://www.sciencedirect.com/science/article/pii/S1000936114002064.

[13] B. Manickam, J. Franke, S.P. Muppala, F. Dinkelacker, Large-eddy simulation of triangular-stabilized lean premixed turbulent flames: Quality and error assessment, Flow Turbul. Combust. 88 (4) (2012) 563–596.

[14] I.B. Celik, Z.N. Cehreli, I. Yavuz, Index of Resolution Quality for Large Eddy Simulations, J. Fluids Eng. 127 (5) (2005) 949–958, http://dx.doi.org/10.1115/1.1990201.

[15] P. Sagaut, Large Eddy Simulation for Incompressible Flows: An Introduction, Springer Science & Business Media, 2006.

[16] J. Pelmard, S. Norris, H. Friedrich, LES grid resolution requirements for the modelling of gravity currents, Comput. & Fluids 174 (2018) 256–270, URL https://www.sciencedirect.com/science/article/pii/S0045793018304407.

[17] E. Aristodemou, T. Bentham, C. Pain, R. Colvile, A. Robins, H. ApSimon, A comparison of mesh-adaptive LES with wind tunnel data for flow past buildings: Mean flows and velocity fluctuations, Atmos. Environ. 43 (39) (2009) 6238–6253, URL https://www.sciencedirect.com/science/article/pii/S1352231009006049.

[18] J. Smagorinsky, General circulation experiments with the primitive equations: I. The basic experiment, Monthly Weather Rev. 91 (3) (1963) 99–164.

[19] J.R. Bull, M.D. Piggott, C.C. Pain, A finite element LES methodology for anisotropic inhomogeneous meshes, in: THMT-12. Proceedings of the Seventh International Symposium on Turbulence Heat and Mass Transfer, Begel House Inc., 2012.

[20] J.H. Ferziger, M. Perić, R.L. Street, Turbulent flows, in: Computational Methods for Fluid Dynamics, Springer International Publishing, Cham, 2020, pp. 347–419.

[21] W. Malalasekera, Turbulence and its modelling, in: An introduction to computational fluid dynamics: the finite volume method, PEARSON Prentice Hall, 2007.

[22] J. O'Neill, X.-M. Cai, R. Kinnersley, A generalised stochastic backscatter model: Large-eddy simulation of the neutral surface layer, Q. J. R. Meteorol. Soc. 141 (692) (2015) 2617–2629.

[23] S. Pope, Large-eddy simulation using projection onto local basis functions, in: J.L. Lumley (Ed.), Fluid Mechanics and the Environment: Dynamical Approaches, Springer Berlin Heidelberg, Berlin, Heidelberg, 2001, pp. 239–265.

[24] J.H.T. Bentham, Microscale Modelling of Air Flow and Pollutant Dispersion in the Urban Environment (Ph.D. thesis), Imperial College London (University of London), 2004.

[25] M. Germano, U. Piomelli, P. Moin, W.H. Cabot, A dynamic subgrid-scale eddy viscosity model, Phys. Fluids A: Fluid Dyn. 3 (7) (1991) 1760–1765, http://dx.doi.org/10.1063/1.857955.

[26] J. Kleissl, Field Experimental Study of the Smagorinsky Model and Application to Large Eddy Simulation, The Johns Hopkins University, 2004.

[27] G.-W. Zou, H.-P. Tan, W.-K. Chow, Y. Gao, Effects of varying smagorinsky constant on simulating post-flashover fires, Int. J. Comput. Fluid Dyn. 21 (2) (2007) 107–119.

[28] C. Chow, W.K. Chow, S. Li, Smagorinsky constant in studying smoke exhaust in a big irregular hall with large eddy simulation, in: ICSDEC 2012: Developing the Frontier of Sustainable Design, Engineering, and Construction, 2013, pp. 375–383.

[29] D.K. Lilly, On the application of the eddy viscosity concept in the inertial sub-range of turbulence, vol. 123, 1966, NCAR manuscript.

[30] J.W. Deardorff, On the magnitude of the subgrid scale eddy coefficient, J. Comput. Phys. 7 (1) (1971) 120–133, URL https://www.sciencedirect.com/science/article/pii/0021999171900532.

[31] V.M. Canuto, Y. Cheng, Determination of the Smagorinsky–Lilly constant CS, Phys. Fluids 9 (5) (1997) 1368–1378, http://dx.doi.org/10.1063/1.869251.

[32] E. Bou-Zeid, C. Meneveau, M. Parlange, A scale-dependent Lagrangian dynamic model for large eddy simulation of complex turbulent flows, Phys. Fluids 17 (2) (2005) 025105, http://dx.doi.org/10.1063/1.1839152.

[33] R. Stoll, F. Porté-Agel, Large-eddy simulation of the stable atmospheric boundary layer using dynamic models with different averaging schemes, Bound.-Lay. Meteorol. 126 (2008) 1–28.

[34] W.-H. Chung, Dependence of the Smagorinsky-Lilly's Constant on Inertia, Wind Stress, and Bed Roughness for Large Eddy Simulations, J. Mech. 22 (2) (2011) 125–136, http://dx.doi.org/10.1017/S1727719100004421.

[35] L. Fang, A new dynamic formula for determining the coefficient of Smagorinsky model, Theor. Appl. Mech. Lett. 1 (3) (2011) 032002, URL https://www.sciencedirect.com/science/article/pii/S2095034915300490.

[36] T. Knopp, X. Zhang, R. Kessler, G. Lube, Enhancement of an industrial finite-volume code for large-eddy-type simulation of incompressible high Reynolds number flow using near-wall modelling, Comput. Methods Appl. Mech. Engrg. 199 (13) (2010) 890–902, Turbulence Modeling for Large Eddy Simulations, URL https://www.sciencedirect.com/science/article/pii/S0045782509000358.

[37] J. Meyers, P. Sagaut, On the model coefficients for the standard and the variational multi-scale Smagorinsky model, J. Fluid Mech. 569 (2006) 287–319.

[38] M. Meldi, D. Lucor, P. Sagaut, Is the Smagorinsky coefficient sensitive to uncertainty in the form of the energy spectrum? Phys. Fluids 23 (12) (2011) 125109, http://dx.doi.org/10.1063/1.3663305.

[39] E.R. Van Driest, On turbulent flow near a wall, J. Aeronaut. Sci. 23 (11) (1956) 1007–1011.

[40] F. Nicoud, F. Ducros, Subgrid-scale stress modelling based on the square of the velocity gradient tensor, Flow Turbul. Combust. 62 (3) (1999) 183–200, Cited by: 2338, URL https://www.scopus.com/inward/record.uri?eid=2-s2.0-0033296193&doi=10.1023%2FA%3a1009995426001&partnerID=40&md5=33272e3e02a486157728900b0b4c9112.

[41] A.W. Vreman, An eddy-viscosity subgrid-scale model for turbulent shear flow: Algebraic theory and applications, Phys. Fluids 16 (10) (2004) 3670–3681, http://dx.doi.org/10.1063/1.1785131.

[42] P. Moin, J. Kim, Numerical investigation of turbulent channel flow, J. Fluid Mech. 118 (1982) 341–377.

[43] U. Piomelli, P. Moin, J.H. Ferziger, Model consistency in large eddy simulation of turbulent channel flows, Phys. Fluids 31 (7) (1988) 1884–1891, URL https://aip.scitation.org/doi/abs/10.1063/1.866635.

[44] G.G. Stokes, On the Effect of the Internal Friction of Fluids on the Motion of Pendulums, Trans. Cambr. Philos. Soc. 9 (1851) 8.

[45] C. Pain, A. Umpleby, C. De Oliveira, A. Goddard, Tetrahedral mesh optimisation and adaptivity for steady-state and transient finite element calculations, Comput. Methods Appl. Mech. Engrg. 190 (29) (2001) 3771–3796.

[46] M.D. Piggott, P.E. Farrell, C.R. Wilson, G.J. Gorman, C.C. Pain, Anisotropic mesh adaptivity for multi-scale ocean modelling, Philos. Trans. A Math. Phys. Eng. Sci. 367 (1907) (2009) 4591–4611, http://dx.doi.org/10.1098/rsta.2009.0155.

[47] M.S. Chong, A.E. Perry, B.J. Cantwell, A general classification of three-dimensional flow fields, Phys. Fluids A: Fluid Dyn. 2 (5) (1990) 765–777, http://dx.doi.org/10.1063/1.857730.

[48] O.R.H. Buxton, M. Breda, X. Chen, Invariants of the velocity-gradient tensor in a spatially developing inhomogeneous turbulent flow, J. Fluid Mech. 817 (2017) 1–20.

[49] J.C. Hunt, A.A. Wray, P. Moin, Eddies, streams, and convergence zones in turbulent flows, in: Studying Turbulence using Numerical Simulation Databases, 2. Proceedings of the 1988 Summer Program, 1988.

[50] C.B. da Silva, J.C.F. Pereira, Invariants of the velocity-gradient, rate-of-strain, and rate-of-rotation tensors across the turbulent/nonturbulent interface in jets, Phys. Fluids 20 (5) (2008) 055101, http://dx.doi.org/10.1063/1.2912513.

[51] M.D. Piggott, G.J. Gorman, C.C. Pain, P.A. Allison, A.S. Candy, B.T. Martin, M.R. Wells, A new computational framework for multi-scale ocean modelling based on adapting unstructured meshes, Internat. J. Numer. Methods Fluids 56 (8) (2008) 1003–1015.

[52] I.C.L. AMCG, Fluidity Manual v4.1.12, figshare, 2015, URL https://figshare.com/articles/journal_contribution/Fluidity_Manual/1387713/2.

[53] R.L. Panton, Incompressible Flow, John Wiley & Sons, 2013.

[54] J.-S. Wu, G.M. Faeth, Sphere wakes in still surroundings at intermediate Reynolds numbers, AIAA J. 31 (8) (1993) 1448–1455, http://dx.doi.org/10.2514/3.11794.

[55] A.G. Tomboulides, Direct and Large Eddy Simulation of Wake Flows: Flow Past a Sphere, Princeton University, 1993.

[56] A.G. Tomboulides, S.A. Orszag, Numerical investigation of transitional and weak turbulent flow past a sphere, J. Fluid Mech. 416 (2000) 45–73.

[57] I. Rodriguez, R. Borell, O. Lehmkuhl, C.D.P. Segarra, A. Oliva, Direct numerical simulation of the flow over a sphere at Re=3700, J. Fluid Mech. 679 (2011) 263–287.

[58] A. Pal, S. Sarkar, A. Posa, E. Balaras, Direct numerical simulation of stratified flow past a sphere at a subcritical Reynolds number of 3700 and moderate Froude number, J. Fluid Mech. 826 (2017) 5–31.

[59] H. Schlichting, Boundary Layer Theory, Vol. 121, Springer, 1961.

[60] E. Achenbach, Experiments on the flow past spheres at very high Reynolds numbers, J. Fluid Mech. 54 (3) (1972) 565–575.

[61] R. Deshpande, A. Desai, V. Kanti, S. Mittal, Experimental investigation of boundary layer transition in flow past a bluff body, J. Phys.: Conf. Ser. 822 (1) (2017) 012003.

[62] K. Ceylan, A. Altunbaş, G. Kelbaliyev, A new model for estimation of drag force in the flow of Newtonian fluids around rigid or deformable particles, Powder Technol. 119 (2) (2001) 250–256, URL https://www.sciencedirect.com/science/article/pii/S0032591001002613.

[63] R. Clift, J.R. Grace, M.E. Weber, Bubbles, Drops, and Particles, Courier Corporation, 2005.

[64] J. Almedeij, Drag coefficient of flow around a sphere: Matching asymptotically the wide trend, Powder Technol. 186 (3) (2008) 218–223, URL https://www.sciencedirect.com/science/article/pii/S0032591007006225.

[65] F.A. Morrison, An Introduction to Fluid Mechanics, Cambridge University Press, 2013.

[66] M. Geier, A. Pasquali, M. Schönherr, Parametrization of the cumulant lattice Boltzmann method for fourth order accurate diffusion part II: Application to flow around a sphere at drag crisis, J. Comput. Phys. 348 (2017) 889–898, URL https://www.sciencedirect.com/science/article/pii/S0021999117305065.

[67] C. Liu, Y. Wang, Y. Yang, Z. Duan, New Omega vortex identification method, Sci. Chin. Phys. Mech. Astron. 59 (8) (2016) 1–9.

[68] T. Nagata, T. Nonomura, S. Takahashi, K. Fukuda, Direct numerical simulation of subsonic, transonic and supersonic flow over an isolated sphere up to a Reynolds number of 1000, J. Fluid Mech. 904 (2020) A36, http://dx.doi.org/10.1017/jfm.2020.629.

[69] M. Geier, M. Schönherr, A. Pasquali, M. Krafczyk, The cumulant lattice Boltzmann equation in three dimensions: Theory and validation, Comput. Math. Appl. 70 (4) (2015) 507–547, URL https://www.sciencedirect.com/science/article/pii/S0898122115002126.

[70] H. Werlé, Onera photograph, in: An Album of Fluid Motion, Assembled By M. Van Dyke, Parabolic Press, Stanford, CA, 1980.

[71] S. Taneda, Visual observations of the flow past a sphere at Reynolds numbers between 104 and 106, J. Fluid Mech. 85 (1) (1978) 187–192.

[72] I. Rodríguez, O. Lehmkuhl, R. Borrell, A. Oliva, Flow dynamics in the turbulent wake of a sphere at sub-critical Reynolds numbers, Comput. & Fluids 80 (2013) 233–243, Selected contributions of the 23rd International Conference on Parallel Fluid Dynamics ParCFD2011, URL https://www.sciencedirect.com/science/article/pii/S0045793012000965.